SANDIA REPORT SAND83—2004 • Unlimited Release • UC—13
Printed October 1983

SAND--83-2004
DE84 003726

Dynamic Fragmentation of Ferroelectric Ceramics Using the Torsional Kolsky Bar

Laurence S. Costin, Dennis E. Grady

Prepared by
Sandia National Laboratories
Albuquerque, New Mexico 87185 and Livermore, California 94550
for the United States Department of Energy
under Contract DE-AC04-76DP00789

Issued by Sandia National Laboratories, operated for the United States Department of Energy by Sandia Corporation.

Printed in the United States of America
Available from
National Technical Information Service
U.S. Department of Commerce
5285 Port Royal Road
Springfield, VA 22161

NTIS price codes
Printed copy: A03
Microfiche copy: A01

Distribution
Category UC–13

SAND83-2004
Unlimited Release
Printed October 1983

Dynamic Fragmentation of Ferroelectric Ceramics Using the Torsional Kolsky Bar

L. S. Costin
Geomechanics Division 1542

D. E. Grady
Thermomechanical and Physical Division 1534
Sandia National Laboratories
Albuquerque, New Mexico 87185

ABSTRACT

In this paper we study the dynamic loading and subsequent fragmentation of four different lead zirconate titanate (95/5 PZT) ferroelectric ceramics using a torsional Kolsky bar apparatus. This study is part of an ongoing effort to better understand the dynamic behavior of ferroelectric materials and the results presented here represent a progress report on our efforts to date. In our experiments, solid cylinders of the four materials were loaded in torsion at shear strain rates in the range 10^2 to $10^3 s^{-1}$. Using the strain gage recordings of the incident, reflected and transmitted pulses, the energy required to fragment the specimen was determined for each test. In addition, the fragments resulting from each test were collected and analyzed by various techniques to determine their mass and size distributions. Our results show some differences in particle distributions between the different batches of material. However, there is a more significant and consistent difference between the dynamic strength (as measured by the maximum shear stress) and the fragment mass distributions of the virgin material and the pressure depoled material, despite the fact that no differences were detected in the energy of fragmentation. Using some earlier analytical results which relate the local kinetic energy of a potential fragment to the surface energy required to create that fragment, a relationship between the distribution of fragments from a test and material properties was derived. The results of our tests on PZT as well as other materials such as oil shale, graphite, uranium dioxide and glass indicate a good correlation between the fragment distribution parameter, n, and material properties as predicted by the theory. Finally, the results are analyzed to determine the potential effects of internal stresses on the dynamic strength of the material and its fragmentation characteristics.

Contents

1 Introduction

Very rapid loading of a brittle material usually results in failure by the nucleation and growth of a large number of fractures. Because large numbers of rapidly growing and interacting cracks are involved, the problem is very difficult to treat using classical fracture mechanics and, thus, statistical or more general energy methods must be used. In this report we present the results of our initial study of the dynamic loading and subsequent fragmentation of four different batches of lead zirconate titanate (PZT) ferroelectric ceramic using a torsional Kolsky bar apparatus. The purpose of these experiments is two fold. First, to determine if there are any demonstrable differences in dynamic mechanical behavior between material which performs well in power supply qualification tests ("good" material) and material which fails the qualification test ("bad" material). Second, to use the data generated by these tests to assist in the evaluation of current theories of dynamic fracture and fragmentation of brittle materials, which may lead to an understanding of the relative differences between good and bad material.

A detailed analysis of the results of the experiments described here has demonstrated that there is a clear connection between quasi-static material properties such as fracture toughness and the distribution of fragments (indicative of the number and size of active flaws in the material) which result from a dynamic loading. In addition, and possibly of more relevance to the power supply problem, there is some indication that internal stresses, which arise in the material because of the ferroelectric to antiferroelectric phase change, are an important factor in determining the dynamic strength of the material.

2 Experimental Procedure

2.1 Test Specimens

Four different batches of 95/5 PZT manufactured by Honeywell were tested. The specimens used in these tests are solid cylinders with integral flanges at each end which are acoustically impedance matched to the Kolsky bars and are used to cement the specimen in place (Figure 1). The nominal specimen dimensions are 10mm in diameter by 7.5mm in length. Table 1 gives the designation and material properties of the four batches of material used. Specimens from each of the four batches were tested in the virgin (as received) and the pressure depoled conditions. The virgin samples were tested at four temperatures: 75, 25, -35, and -60 °C. The pressure depoled specimens were tested at room temperature only. Pressure depoling consisted of hydrostatically stressing the specimen to approximately 480 MPa. The ferroelectric to antiferroelectric phase change occurs at approximately 275 MPa [1].

2.2 Kolsky Bar Apparatus

Since a complete description of the apparatus and experimental procedure has been documented previously [2,3], only a brief account is given here. Referring to Figure 2, the sudden opening of the clamp at B releases the torque stored in the input bar between A and B. The torsional pulse propagates from the clamping point and interacts with the specimen which is bonded between the input and transmitter bars at point C. The wave interaction at the specimen results in a portion of the input pulse being transmitted through the specimen with the remainder being reflected back into the input bar. Strain gages at D and E sense the incident, reflected and transmitted pulses which are recorded with a digital oscilloscope. These time-resolved stress pulse measurements are then used to calculate the torque history as well as the work done on the specimen during the test. Note that because we use solid cylinders instead of the more traditional thin-walled tubes, both the stress and strain vary along the radius of the specimen. Thus, we can only compute the approximate maximum stress and strain which occur at the outer surface of the specimen.

Table 1. Material Properties of PZT Specimens.

Batch	ρ Kg/m^3	E GPa	ν	K_{Ic} MPa$\sqrt{m}$	C_o Km/s	C_s Km/s
4123A	7,371	114	.21	1.38	4.18	2.53
4122S	7,295	112	.21	1.47	4.15	2.52
3507S	7,427	110	.19	1.59	4.04	2.49
3922S	7,253	110	.22	1.22	4.14	2.49

Using an analysis paralleling that of Kolsky [4] for the compressional bar, it can be shown that the torque applied to the specimen is equal to the transmitted torque recorded in the transmitter bar (T_2). The rate of rotation applied to the specimen ($\dot{\theta}$) is proportional to the reflected pulse (T_3). This is expressed as

$$\dot{\theta} = \frac{2T_3(t)}{\rho JC} \tag{1}$$

where the product ρJC is the torsional impedance of the elastic bars, ρ being the density, J the polar moment of inertia, and C the shear wave velocity. The work done on the specimen up to time t ($E(t)$) is given by

$$E(t) = \frac{2}{\rho JC}\int_0^t T_2 T_3 dt \tag{2}$$

The strain rate imposed on the specimen during the test is controlled by the magnitude of the input pulse. For all tests reported here the input pulse was set at a torque of 120N-m. This resulted in an average strain rate in the specimen of $500s^{-1}$. Before testing, each specimen was enclosed in an aluminum foil cylinder which was sealed against the loading bars. The foil cylinder served as a catching tank for the fragments which were created during the test. After the test was complete the foil was removed and the fragments were carefully transferred to a clean glass jar.

To achieve test temperatures below nominal room temperature, an insulated box was placed around the central portion of the bar system containing the

specimen. A controlled flow of liquid nitrogen was used to cool the specimen. For elevated temperature tests, a small quartz lamp furnace was used to heat the specimen. In all cases, the heating or cooling rate was kept below five degrees centigrade per minute in order to prevent large thermal stresses from damaging the specimen.

2.3 Fragment Distributions

The fragments collected from each test were sieved to determine the fragment size distribution. Five sieves were used in a stack and an ultrasonic shaker was used to agitate the sieves to insure the separation of sizes was complete. The sieve sizes used ranged geometrically from $2000\mu m$ down to $125\mu m$. The mass of particles retained in each sieve was weighed to provide a mass distribution of the fragments. In most cases, approximately 35% of the mass was retained in the largest sieve. In order to provide a complete distribution for one set of data, the fragments from tests conducted at room temperature on both the virgin and the pressure depoled materials were subjected to a more complete analysis. For this, particles larger than $2000\mu m$ were weighed individually. To estimate the size of the larger particles, it was assumed that they were nearly spherical and thus the size (D) of each particle was assumed to be given by

$$D = 2\left(\frac{3m_p}{4\pi\rho}\right)^{\frac{1}{3}} \tag{3}$$

where m_p is the mass of a particle and ρ is the density.

3 Results

3.1 Test Records

Figure 3 shows the strain gage records and the integrated energy (equation (2)) for a typical test. Referring to the transmitted pulse in Figure 3, it appears that two distinct processes occur during the test. First, the specimen loads elastically for 15 to 20μs up to a peak stress where it appears that an initial failure occurs. We interpret this peak stress point as being the point where fractures from the most critically loaded flaws initiate and propagate, resulting in sudden drop in the load carrying capacity of the specimen. The load supported by the specimen is not relieved completely at this point, however, because many of the particles created by this initial burst of fractures continue to be held in place by inertial and geometric constraints. Further imposed deformation is accomodated by sliding along fracture surfaces and fragment rotation, creating secondary fragmentation. This "grinding" process continues for approximately 200μs until enough of the specimen has fallen away to cause a complete loss of load transfer into the transmitter bar. Thus, the material in the specimen first fractures (this is referred to as prompt fragmentation) and then is subjected to secondary breakage during the comminution phase of the test.

The energy consumed in the fragmentation process is also shown in Figure 3. Note that very little energy is required for prompt fragmentation. Most of the work done on the specimen is done during the comminution phase of the test. In relating the results of these tests to the problems encountered in the failure of power supplies by voltage breakdown, it appears that the prompt fragmentation portion of the test record is probably of most importance. However, as will be seen later in this report we have tried to make use of the entire test history and response of the material to assess any differences in materials which may be related to their performance under dynamic loading.

3.2 Maximum Stress

The shear stress in the specimen is greatest on the outer surface. Therefore, at the point of maximum transmitted torque (fracture initiation), the maximum

stress supported by the specimen material is given approximately by

$$\tau_{max} = \frac{2T_{2(max)}}{\pi r^3} \tag{4}$$

where r is the radius of the specimen cylinder. τ_{max} is also the maximum tensile stress which occurs at 45° to the cylinder axis. It is these tensile stresses which initiate the fractures. Thus, τ_{max} is a measure of the stress required to initiate a fracture from the most critical flaw.

Figure 4 shows a plot of τ_{max} versus temperature for each of the four materials tested. It is expected that "good" materials should have a relatively high τ_{max} whereas the "bad" materials should have a lower τ_{max}. The 4122S, has the lowest τ_{max} at all test temperatures, consistent with its "bad" rating from the qualification tests. The other three materials are about equal if τ_{max} is averaged over the range of temperatures. However, at -35°C, the temperature at which the most problems in power supply performance have occured, there is a distinct difference between the two "good" materials (3507S and 3922S) and the two "bad" materials (4122S and 4123A). This difference is significant compared to nominal experimental scatter.

A comparison of the maximum shear stress for the virgin and the pressure depoled materials at 25°C is given in Figure 5. It is clear from the figure that there is a consistent difference between the virgin and the pressure depoled material. The strengthening effect of depoling shown in Figure 5 is consistent with the increase in fracture toughness that also accompanies depoling [5].

It has been suggested that large local internal stresses created by the ferroelectric to antiferroelectric phase change, could be a significant contributing factor to the premature failure of the PZT element during dynamic loading [6]. The magnitude of the local internal stress acting on a critical flaw can be estimated using the analysis of Pohanka et al. [6]. The sum of the local internal stress and the applied stress must equal the critical driving force for a flaw of nominal length a. That is

$$\tau + < \sigma_I > = C\frac{K_{Ic}}{\sqrt{a}} \tag{5}$$

where $< \sigma_I >$ is the local internal stress, K_{Ic} is the fracture toughness and C is a constant which accounts for the geometry of flaw and its orientation with respect to the stress field. For a semicircular crack intersecting the surface of the specimen (where the applied stresses are the greatest), C is approximately 1.2. Because equation (5) is only a rough approximation, it seems reasonable only

to make a relative comparison of the internal stress levels associated with each material. Rearranging equation (5) gives

$$\frac{<\sigma_I>}{\tau} \sim \frac{K_{Ic}}{\tau\sqrt{a}}$$

Thus, if the dimensionless parameter $K_{Ic}/\tau\sqrt{a}$ is large, it implies that the internal stresses are large relative to the applied stresses. In contrast, if $K_{Ic}/\tau\sqrt{a}$ is small, it is expected that the internal stresses are small relative to the applied stresses.

Figure 6 shows the internal stress parameter for each material at 25°C. Unfortunately, there was not enough material remaining from the batches tested to determine the fracture toughnesses of each material after pressure depoling. Thus, no comparison of internal stresses in the virgin material with those in the pressure depoled material can be made. However, it is evident from Figure 6 that the internal stresses are of the same order as the applied stresses. In computing the values of the internal stress parameter presented in Figure 6, a was assumed to be $200\mu m$. This value is typical of the flaw size found in many PZT ceramics [7].

3.3 Fragment Analysis

An example of the measured fragment mass distributions for each of the four materials is given in Figure 7. The distribution curves were found to be well described by an expression of the form

$$m = m_o\left(\frac{x}{\sigma}\right)^n \tag{6}$$

where m is the cumulative mass passing size x, σ is the size of largest fragment, n is a constant exponent (shape factor) and m_o is the total mass of fragments. Assuming that the fragments are nearly cubical in shape, the fracture surface area associated with all the fragments of size less than x is given by

$$A(x) = 1.75\left(\frac{6m_o}{\rho\sigma}\right)\left(\frac{n}{n-1}\right)\left(\frac{x}{\sigma}\right)^{n-1} \tag{7}$$

where the factor of 1.75 is an empirical constant determined by Gaudin [8] to account for the geometric irregularities in particle shapes. It should be noted

that equations (6) and (7) above, are strictly applicable only to those distributions which were measured out to the largest particle (room temperature tests). However, similar equations were used to fit the distributions of the other tests where only sieve sizes to $2000\mu m$ were measured. These equations are given in reference [9]. The value of n derived from fitting a complete distribution (equation (6)) and the value derived from fitting only the lower part (below $2000\mu m$) were found to be very nearly equal in all cases.

The shape parameter, n, was found to vary from 1.2 to 1.6 depending on the particular batch of material and the test temperature (Table 2). A small n (near 1.0) indicates a nearly uniform distribution such as might be expected from a comminution process. A larger n (greater than 1.5) indicates the fragment distribution is weighted toward the larger particles and is more indicative of dynamic fragmentation in which little secondary breakage occurs (for example, the fragmentation of an artillery shell). Because of the limited number of specimens available, we were able to perform only a few repeat tests in order to asses the variability of the results. From the multiple tests we did perform under similar conditions, it was determined that the value of n was repeatable to within 7%. Thus, the apparent differences in n between material batches (Figure 7) are significant compared to possible experimental error.

The distributions shown in Figure 7 can each be fit by a single straight line represented by equation (6) with a different n for each material. This is because only a relatively small amount of the mass(less that 35%) was larger than the largest sieve size used to form the distributions ($2000\mu m$). In related work on other materials, we have found that when the mass larger than a certain size, which depends on the specimen size, exceeds 70% of the total fragment mass, a bimodal distribution of fragment mass begins to appear. The smaller fragments have a shape parameter, n, near unity, whereas the larger fragments tend to have a larger shape parameter, $n > 1.5$. Such a distribution, resulting from tests on an isotropic graphic is shown in Figure 8. It appears that for these tests, the large fragments are a result of the prompt fragmentation (at peak stress) and the smaller fragments are the result of subsequent comminution of fragments. For the PZT, all the fragments fit on the same distribution curve (Figure 7), indicating that the low value of n derived from these tests is due, to a great extent, to the very brittle nature of the material and as a consequence, all of the fragments are apparently subjected to a similar comminution history.

3.4 Energy Analysis

The total energy consumed during each test was computed from equation(2). The specific energy or energy per unit of fracture area created during the frag-

Table 2. Summary of Results

Batch/ Temp.	τ_{max} MPa	n	Energy J	Sp Energy J/m^2
4123A				
75°C	55.6	1.47	.340	101
25°C	61.4	1.50	.435	122
-35°C	43.2	1.54	.471	107
-60°C	62.3	1.39	.521	146
4122S				
75°C	45.2	1.28	.599	194
25°C	42.4	1.36	.430	150
-35°C	38.4	1.23	.359	104
-60°C	48.1	1.26	.383	109
3507S				
75°C	48.1	1.37	.418	170
25°C	46.1	1.53	.445	154
-35°C	57.2	1.39	.401	151
-60°C	55.4	1.38	.420	135
3922S				
75°C	64.1	1.35	.479	102
25°C	49.5	1.37	.384	97.8
-35°C	59.0	1.41	.485	96.3
-60°C	70.8	1.32	.323	82.2

mentation was computed by dividing the total energy by the total fragment area (equation(7)). The results of the energy computations are given in Figures 9 through 11 and Table 2. There is far less variability in the fragmentation energy (Figure9) among the four materials tested than was evident in the maximum stress data (Figure 5). In addition there appears to be no correlation between the energy consumed in fragmentation and the test temperature (Figure 10) or the resulting fragment distribution (Figure 11).

Since it appears that the experimental parameters associated with the initial failure of the ferroelectric element should be a better predictor of device performance, an attempt was made to measure the energy associated with the initial failure of the specimen at the point of maximum stress. However, the energy at this point is so small that no accurate measurements could be made. The work done on the specimen up to the point of peak load is essentially stored as elastic energy in the specimen and is negligible compared to the work done in the later portion of the test.

4 Discussion

4.1 Estimation of Fragment Size

From the results of tests presented here, it is evident that the total energy consumed during the fragmentation of a specimen is not very indicative of the resistance of the material to fracture under dynamic loading. The peak stress, τ_{max}, appears to be a better measure of the resistance of the material to dynamic failure but this can be confused by the internal stresses which result from the phase change which occurs on depoling. Thus, it would be useful if we could establish some direct connection between measurable material parameters such as fracture toughness and the dynamic failure properties of a material which can be most easily characterized by the distribution parameter, n. The analysis presented below is an attempt to provide such a connection.

In some recent work, Grady [10] has demonstrated that the size of a fragment created during a dynamic event may be related to the requirement that the particle energy be minimized. Applying Grady's analysis of the fragmentation of a rapidly expanding liquid sphere, we assume that the particle energy is composed of two parts: the local kinetic energy and the energy associated with the newly created fracture surfaces. Consider, prior to fragmentation, an element of

mass within the specimen which will constitute the mass of an average fragment after the fracturing process is completed (Figure 12). When referred to a fixed coordinate system, the total kinetic energy of the potential fragment can be considered to be the sum of the kinetic energy of the center of mass and the kinetic energy relative to the center of mass. If we assume that, during fragmentation, the mass element will experience no net impulse, the kinetic energy of the center of mass must remain constant. Therefore, only the kinetic energy relative to the center of mass is available to drive the fracture process.

For a solid cylinder under torsional loading, the local kinetic energy (about the center of mass) of a potential particle (Figure 12) is related to the rate at which the particle mass is being deformed in shear (rotated). Thus, we can approximate the kinetic energy about the center of mass by

$$T^* = \frac{1}{2} I\omega^2 = \frac{1}{2}(\rho \ell^2 h)\left(\frac{\ell^2}{6}\right)(\dot{\gamma}^2) \tag{8}$$

where the particle is assumed to be a cuboid of side ℓ and thickness h (Figure 12). The surface area of this potential fragment is

$$A = 2\ell^2 + 4\ell h \tag{9}$$

If we define the aspect ratio, α, to be

$$\alpha = \frac{\ell}{h} \tag{10}$$

then the specific area of the particle (area created per unit volume of material) is given by

$$a = \frac{2\alpha + 4}{\ell} \tag{11}$$

Thus, the specific local kinetic energy is given by

$$T = \frac{1}{12}\rho \frac{(2\alpha + 4)^2}{a^2}\dot{\gamma}^2 \tag{12}$$

The surface energy associated with the new fracture surfaces can be approximated using Irwin's relation

$$2\gamma = \frac{K_{Ic}{}^2}{E} \tag{13}$$

where γ is the surface energy and E is Youngs modulus. The factor of two arises because two surfaces are created by each fracture. Combining equations (12) and (13) we have the total specific energy of the fragment

$$e = \frac{\rho(2\alpha+4)^2\dot{\gamma}^2}{12a^2} + \frac{{K_{Ic}}^2}{2E}a \tag{14}$$

The kinetic energy term results in forces which tend to increase fracture surface area whereas the surface energy provides a force resistant to the production of new surface area. As noted above, we assume that during fragmentation, these opposing forces will seek to minimize the local particle energy, equation(14). Therefore, requiring

$$\frac{\partial e}{\partial a} = 0$$

results in

$$a = \left[\frac{E\rho(2\alpha+4)^2\dot{\gamma}^2}{3{K_{Ic}}^2}\right]^{\frac{1}{3}} \tag{15}$$

Equation (15) provides a quantitative measure of the fracture surface area in terms of fundamental material and kinematic properties.

The surface area of fragments created is rather difficult to measure directly. However, we can estimate the surface area from the fragment distribution using equation (7). From equation (7) it is apparent that

$$a \sim \left(\frac{n}{(n-1)\sigma}\right)$$

Table 3. Nominal Properties of Other Materials Tested.

Material	ρ Kg/m^3	E GPa	K_{Ic} MPa$\sqrt{m}$	n
UO_2	10,860	192	1.58	1.51
Glass	2,200	37	.54	1.30
Oil Shale				
10 GPT	2,591	20	1.2	2.09
20 GPT	2,360	15	1.0	2.21
30 GPT	2,140	10	.80	2.86
40 GPT	2,050	6	.65	3.22
Graphite	1,850	12	1.37	2.55

If we assume that the variations in fragment geometry are negligible, then using the above relationship in conjunction with equation (15) yields the relation

$$\frac{n}{n-1} \sim \left(\frac{\sigma^3 E \rho \dot{\gamma}^2}{K_{Ic}{}^2} \right)^{\frac{1}{3}} \tag{16}$$

This relationship gives us a means of evaluating the dynamic fracture characteristics of a material relative to measurable material properties and loading conditions. To demonstrate the potential usefulness of this result, we have tested several materials using the Kolsky bar technique. These materials have a wide range of material properties (ρ, E, and K_{Ic}) as shown in Table 3. Each of the materials was tested using approximately the same specimen configuration and loading rate as used with the PZT. A fragment distribution analysis was done for each test. For materials which fragmented into mostly large particles and showed a bimodal fragment distribution, the shape factor associated with the prompt fragmentation was taken as best describing the distribution. The results of these tests are shown if Figure 13. There is a clear trend to the data indicating that there is a relationship between the fragment size and the dimensionless material parameter as expressed in (16).

This result can also prove useful in evaluating the performance of the PZT in dynamic loading experiments. It is apparent from (16) that material with a low density, low modulus and high fracture toughness has more resistance to fragmentation than high density, high modulus, low fracture toughness material, all other things being equal.

4.2 Future Work

Although the results of these experiments are encouraging, there are several problems which need more attention. Most of these are related to the type of loading used. In the loading of solid cylinders in torsion, neither the stress nor the strain rate in the specimen is uniform, making analysis of the results more difficult. In addition, with brittle materials the primary mode of failure is by the nucleation of tensile cracks along directions of maximum tensile stress. In power supplies, the primary loading occurs in compression and crack growth can occur in directions parallel to the maximum compressive stress. Thus, the results obtained from torsional loading may not be indicative of material behavior under operational conditions.

In our next series of tests, the Kolsky bar will be used to dynamically load small specimens in compression. A gas gun which fires a 25 mm diameter rod will be used to generate short duration axial pulses in the bar system. With axial compression loading, the stress and strain rate are nearly uniform throughout the specimen and can be controlled by controlling the input pulse. Also, by using short impact rods, the effect of pulse duration on the fracture process can be examined in more detail. Finally, the compressive loading more closely approximates the loading which occurs during the operation of a power supply.

References

1. **Fritz, I. J.**
   Uniaxial-Stress Effects in a 95/5 Lead Zirconate Titanate J. App. Phys., Vol. 49, 1978, pp. 4922–4928.
2. **Lipkin, J. and Jones, A. K.**
   Dynamic fracture strength of oil shale under torsional loading, Proceedings 20^{th} US. Symposium on Rock Mechanics, Austin, TX, June, 1979.
3. **Lipkin, J., Schuler, K. W. and Parry, T.**
   Dynamic torsional failure of limestone tubes, Mechanical Properties at High Rates of Strain, 1979, J. Harding, ed., Inst. Phys. Conf. Ser. No. 47, 1979, pp. 101–110.

4. **Kolsky, H.**
An investigation of the mechanical properties of materials at very high rates of loading, Proc. Physical Soc., Vol. 62, 1949, pp. 676–699.
5. **Freiman, S. W.**
Fracture toughness of 95/5 PZT Final Report for FY82 to Sandia National Laboratories.
6. **Pohanka, R. C., Freiman, S. W. and Bender, B. A.**
Effect of the phase transformation on the fracture behavior of $BaTiO_3$, J. Amer. Ceramic Soc., Vol. 61, 1978, pp. 72–75.
7. **Mecholsky, J. J**
Private Communication
8. **Gaudin, A. M.**
Principles of Mineral Dressing McGraw-Hill, New York, 1939
9. **Grady, D. E., Lipkin, J. and Costin, L. S.**
Energy and particle size effects in the fragmentation of oil shale with a torsional split-Hopkinson bar, Proc. 22^{nd} US. Symp. on Rock Mech., MIT, Cambridge, MA, June, 1981.
10. **Grady, D. E.**
Local inertial effects in dynamic fragmentation, J. Appl. Phys., Vol. 53, pp. 322, 1982.

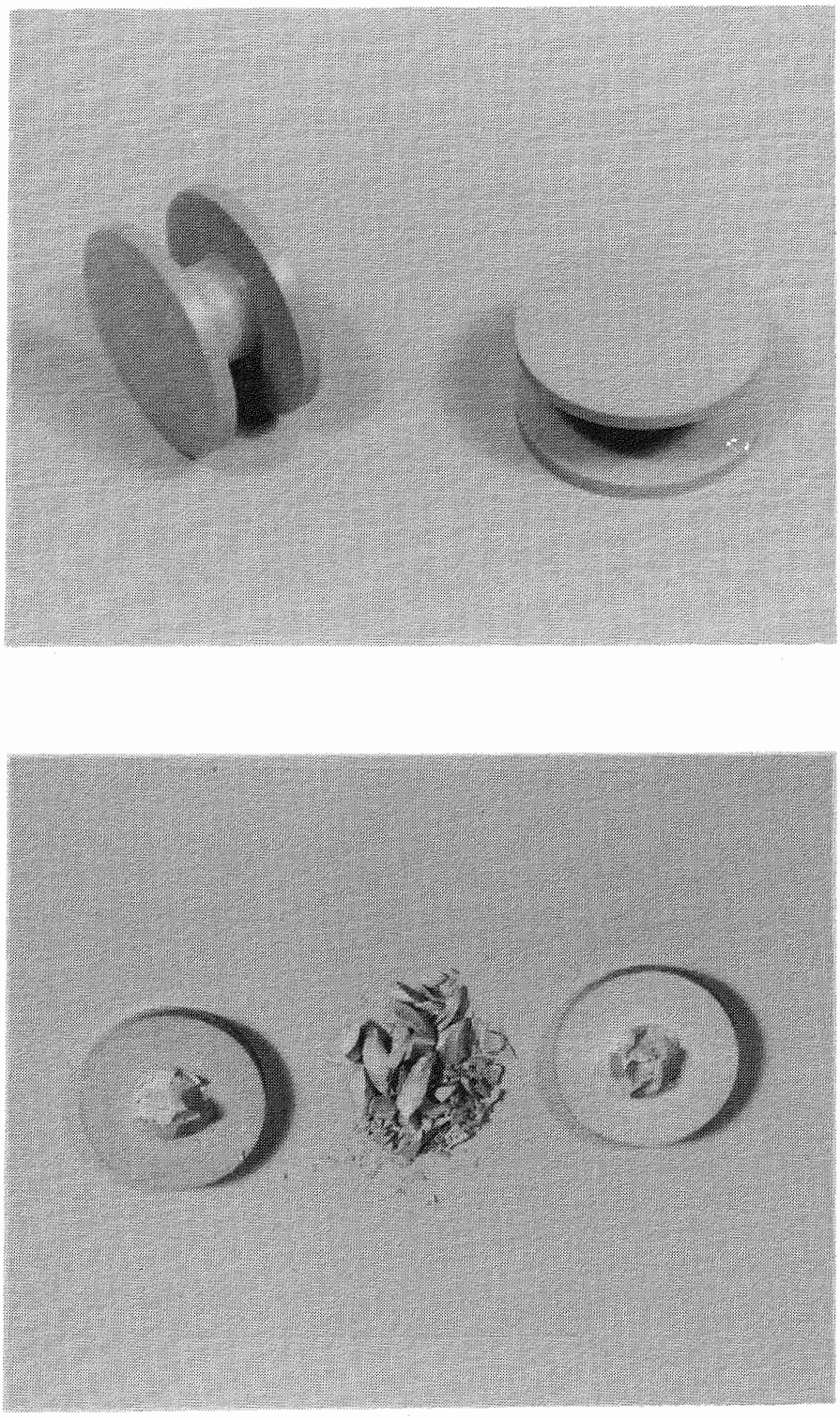

Figure 1

Photograph of typical specimens used in dynamic tests.

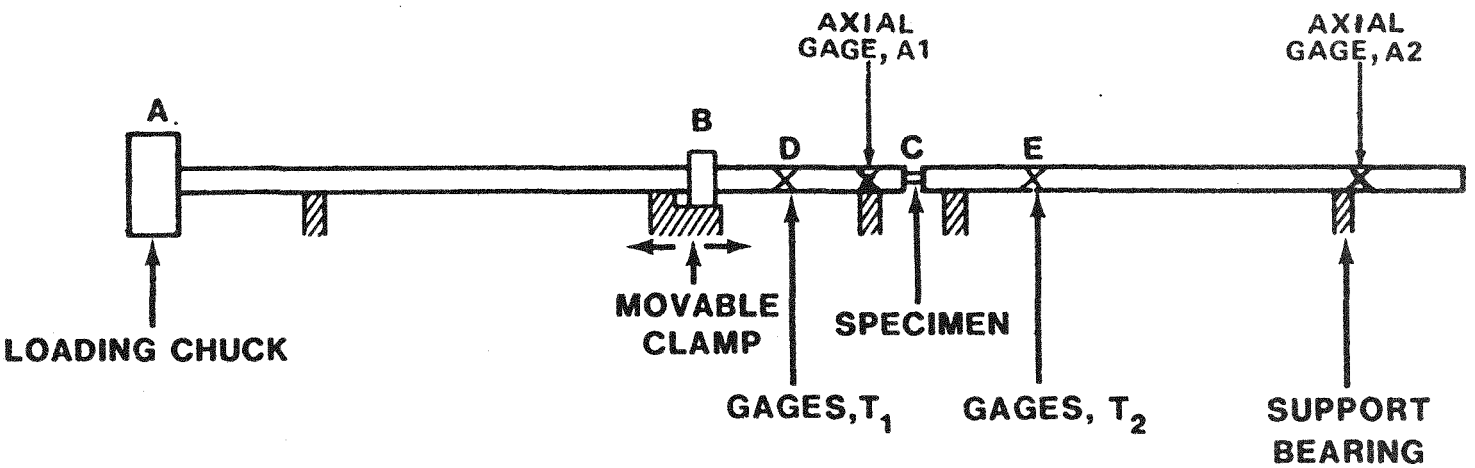

Figure 2

Schematic drawing of Kolsky bar.

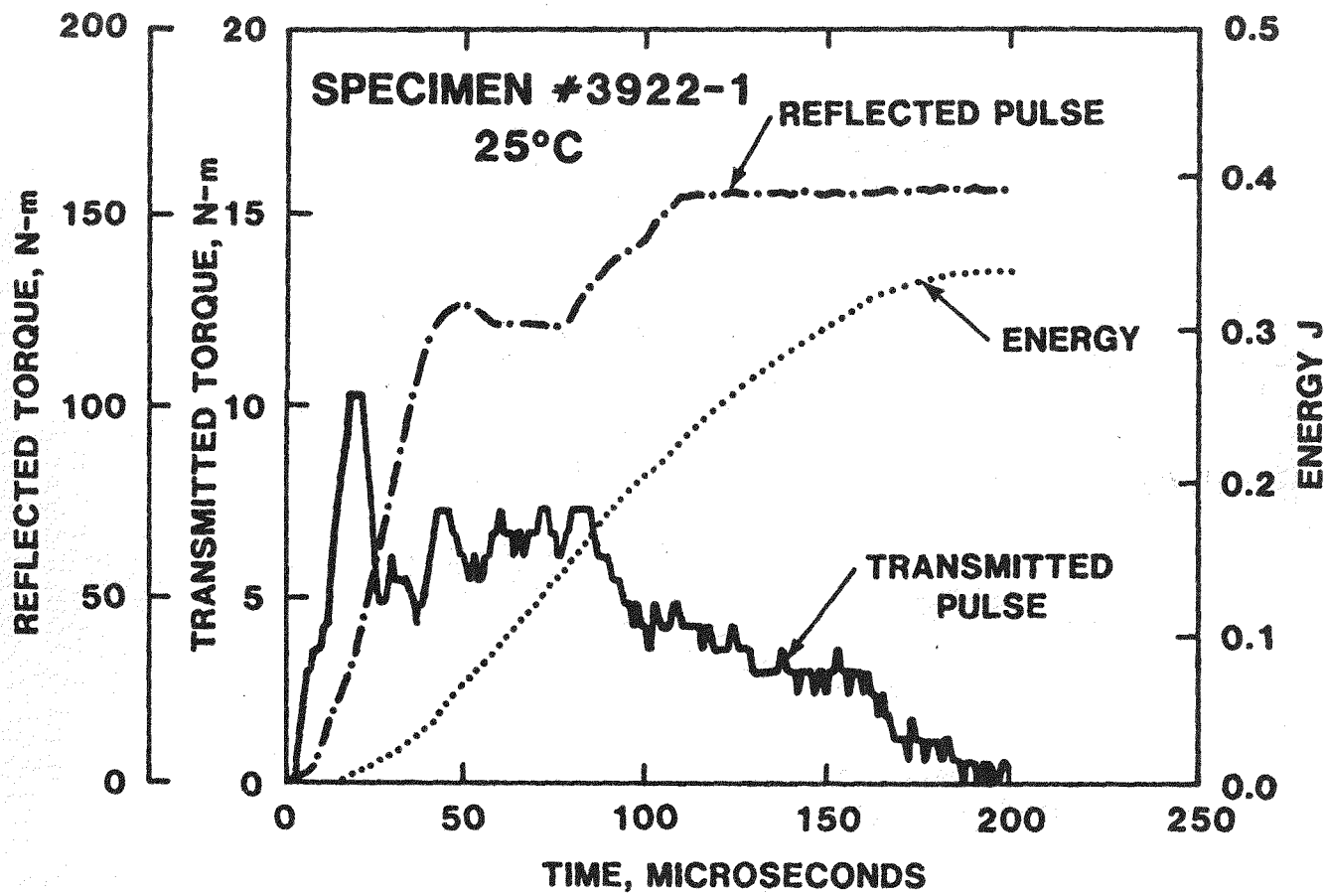

Figure 3

Typical record for fragmentation test showing reflected and transmitted pulses with integrated energy.

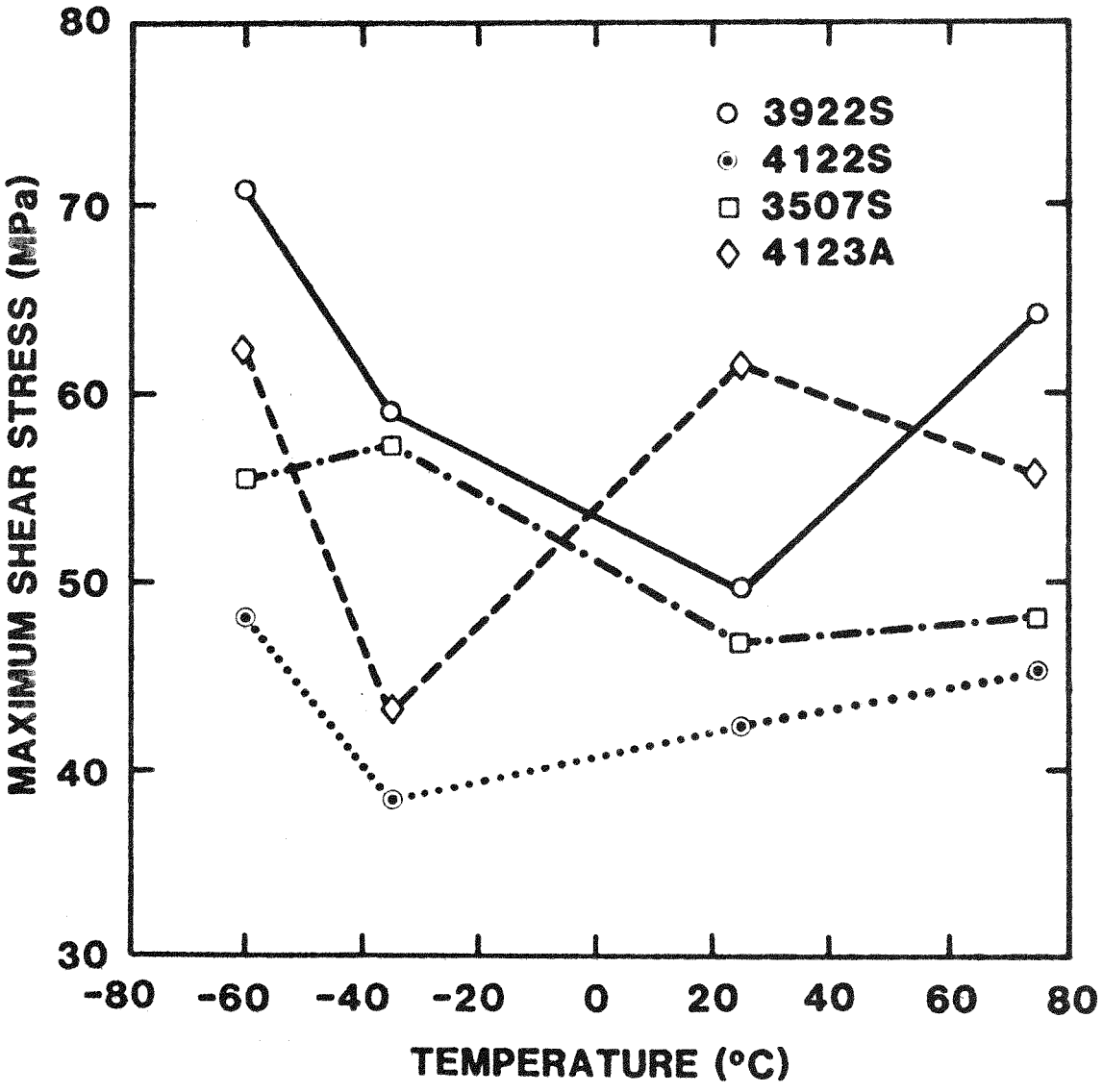

Figure 4

Maximum shear stress (τ_{max}) versus temperature for four batches of PZT

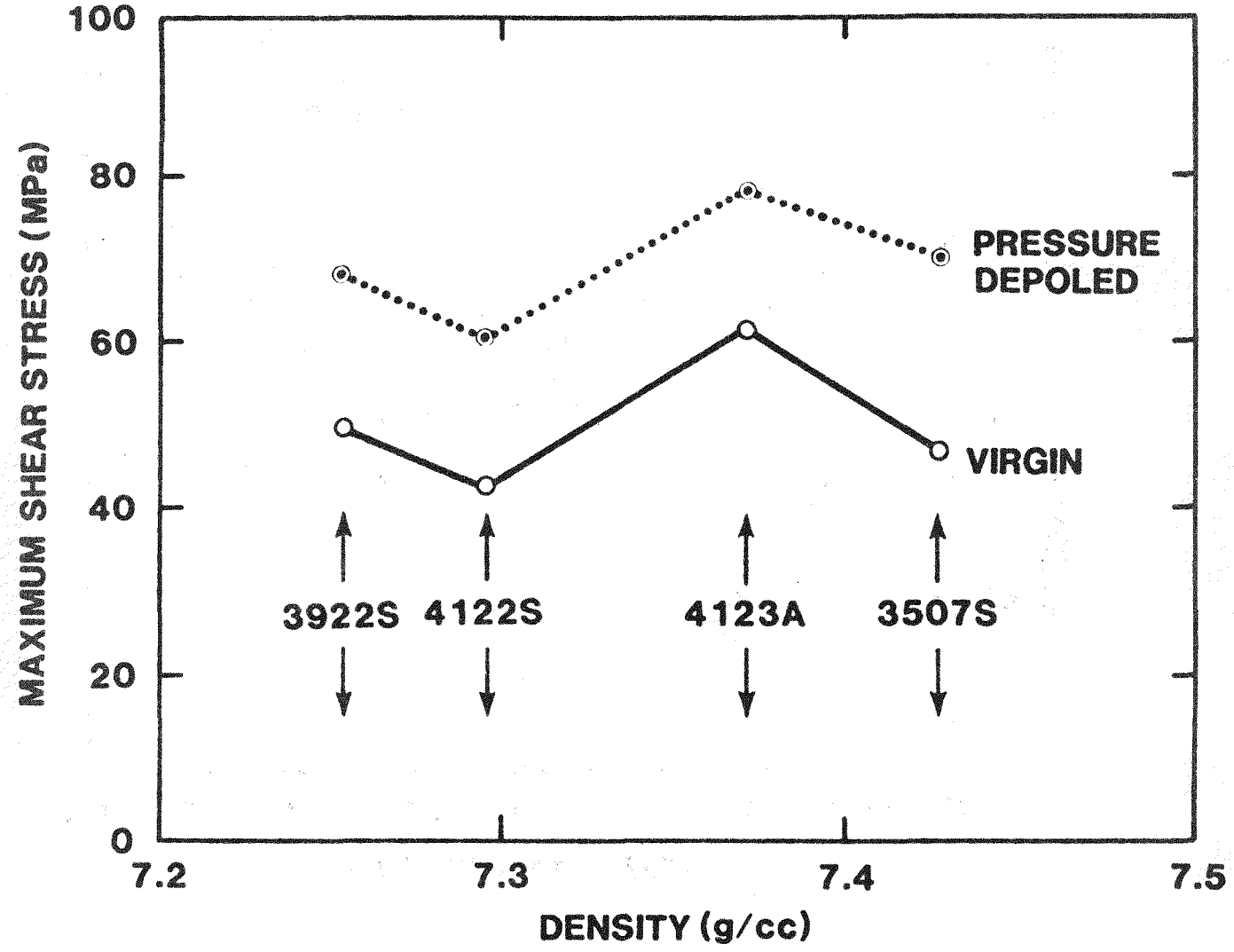

Figure 5

Maximum shear stress (τ_{max}) versus density for the virgin and pressure depoled materials at 25°C.

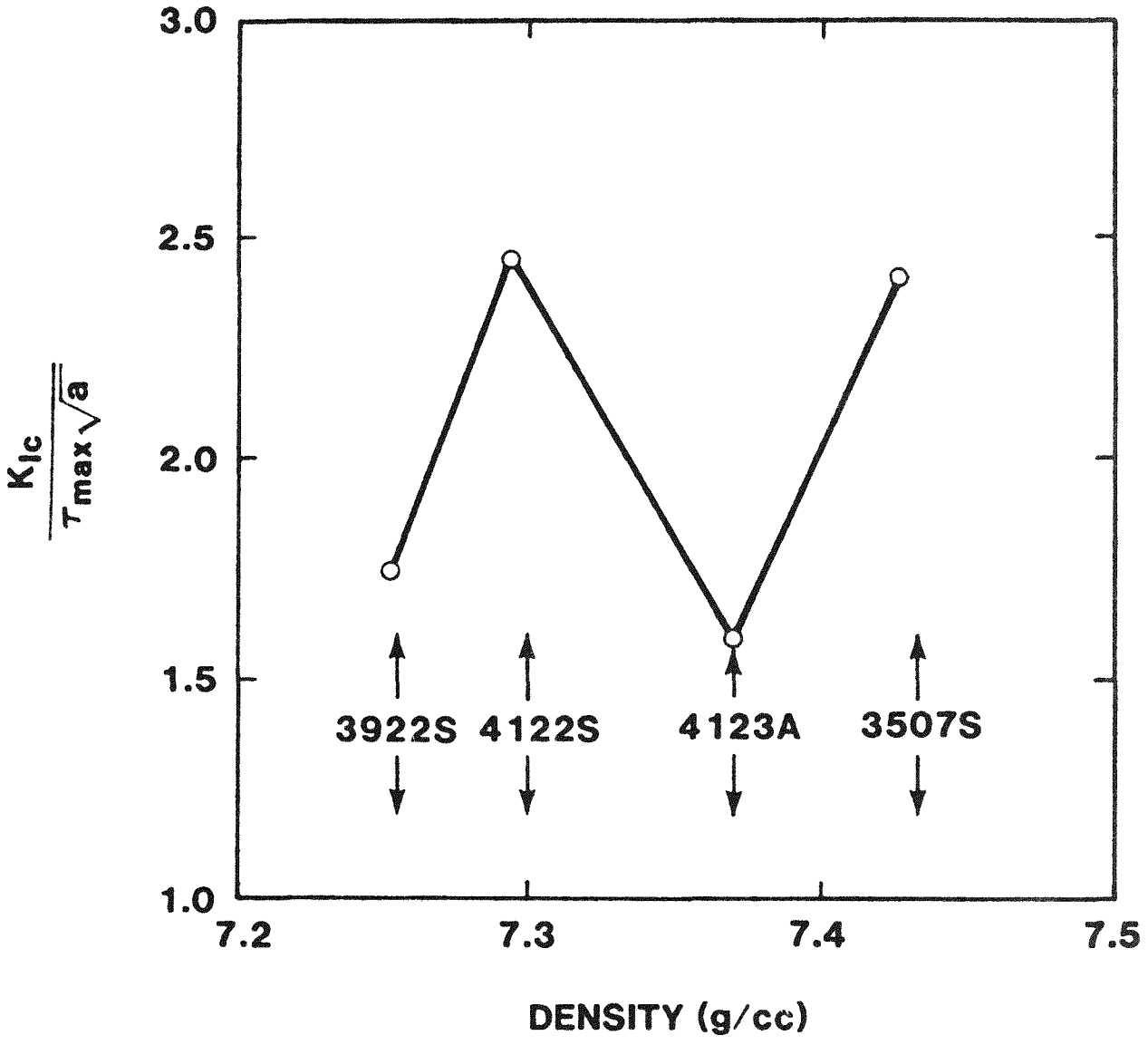

Figure 6

Internal stress parameter versus density for virgin materials at 25°C.

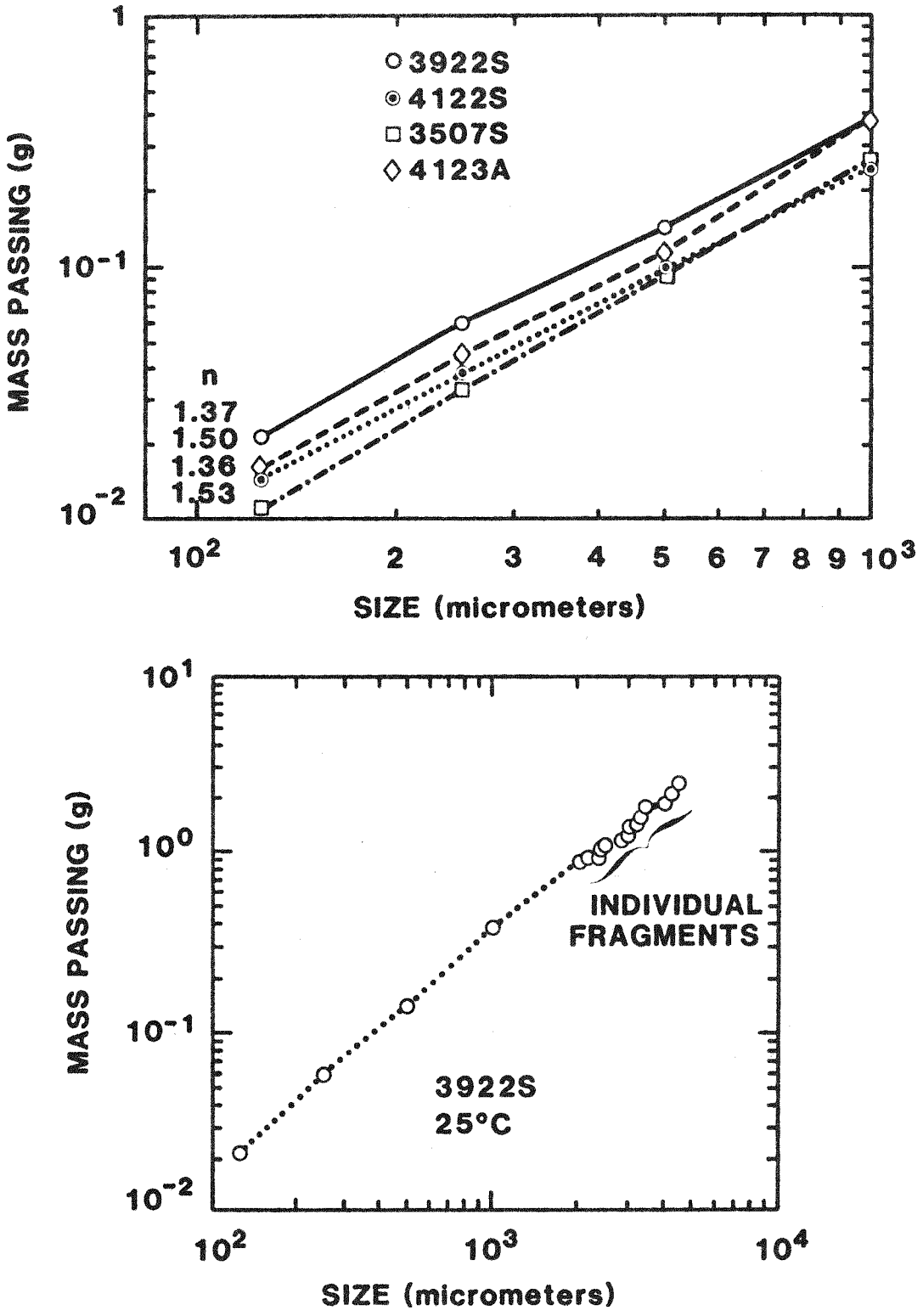

Figure 7

Top: Fragment distributions for each material at 25°C. **Bottom:** Complete fragment distribution for one test.

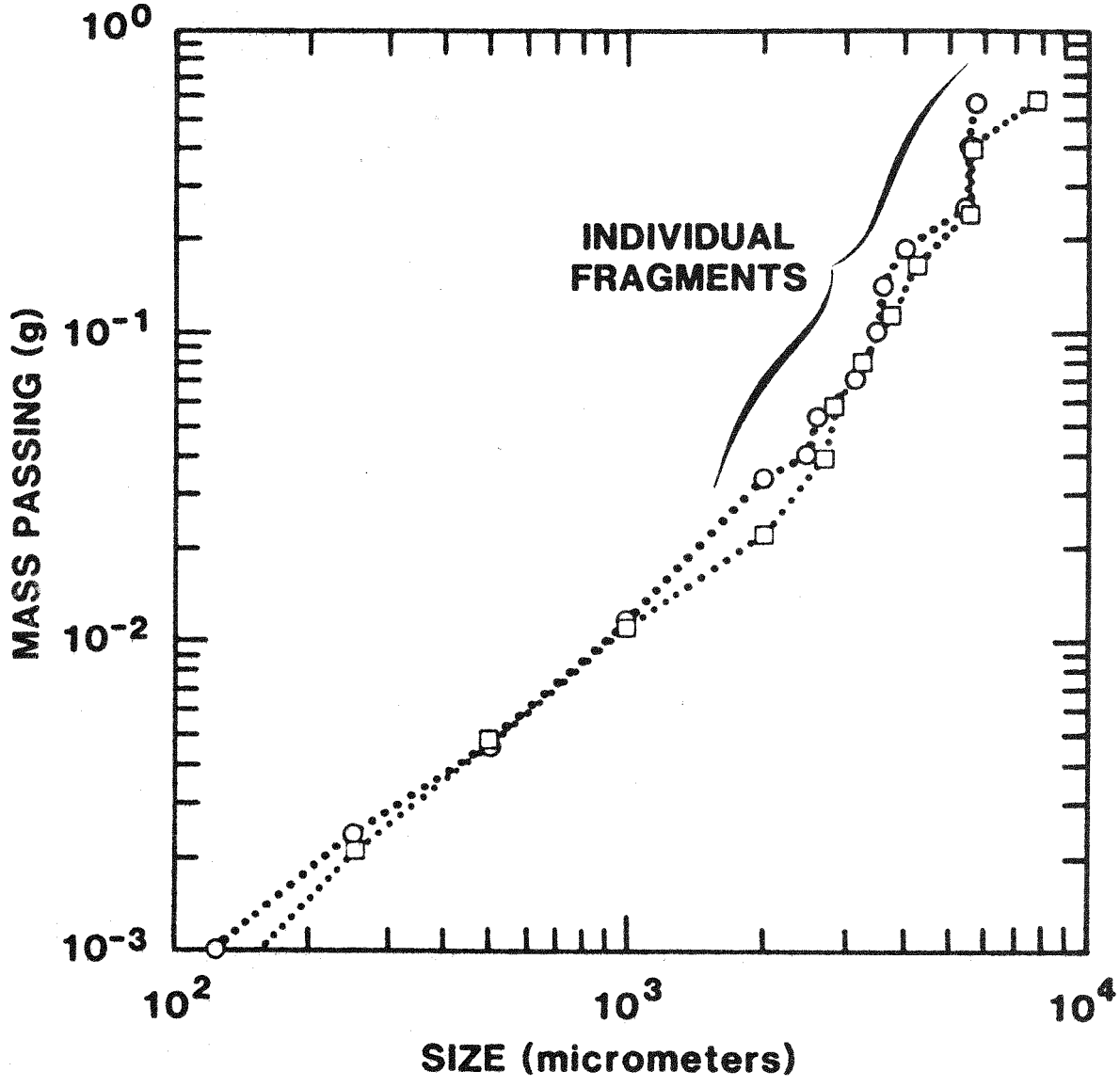

Figure 8

Fragment distribution for isotropic graphite showing bimodal distribution characteristic of prompt fragmentation followed by secondary breakage.

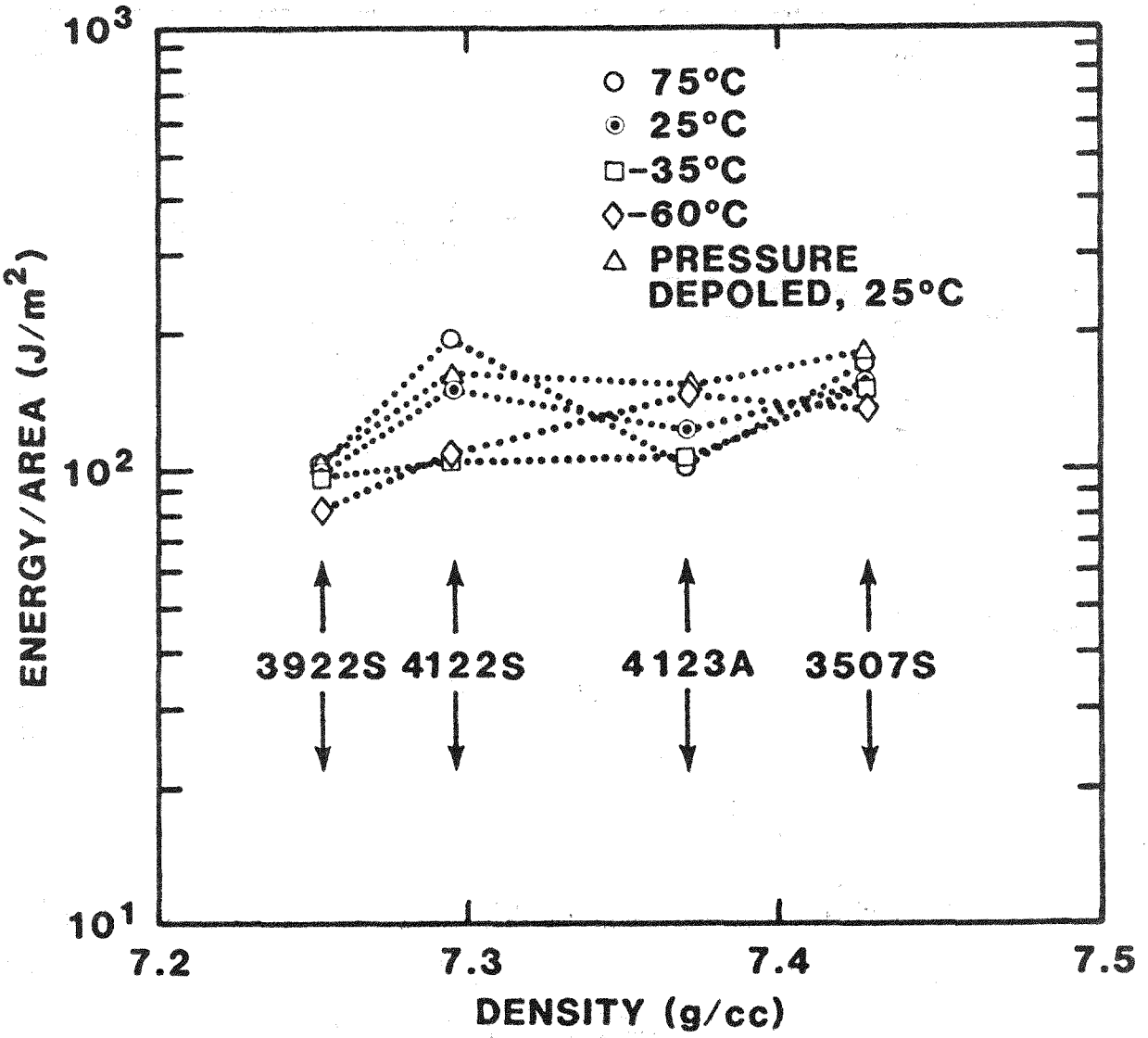

Figure 9

Energy of fragmentation versus density for virgin materials at four different temperatures and pressure depoled materials at room temperature.

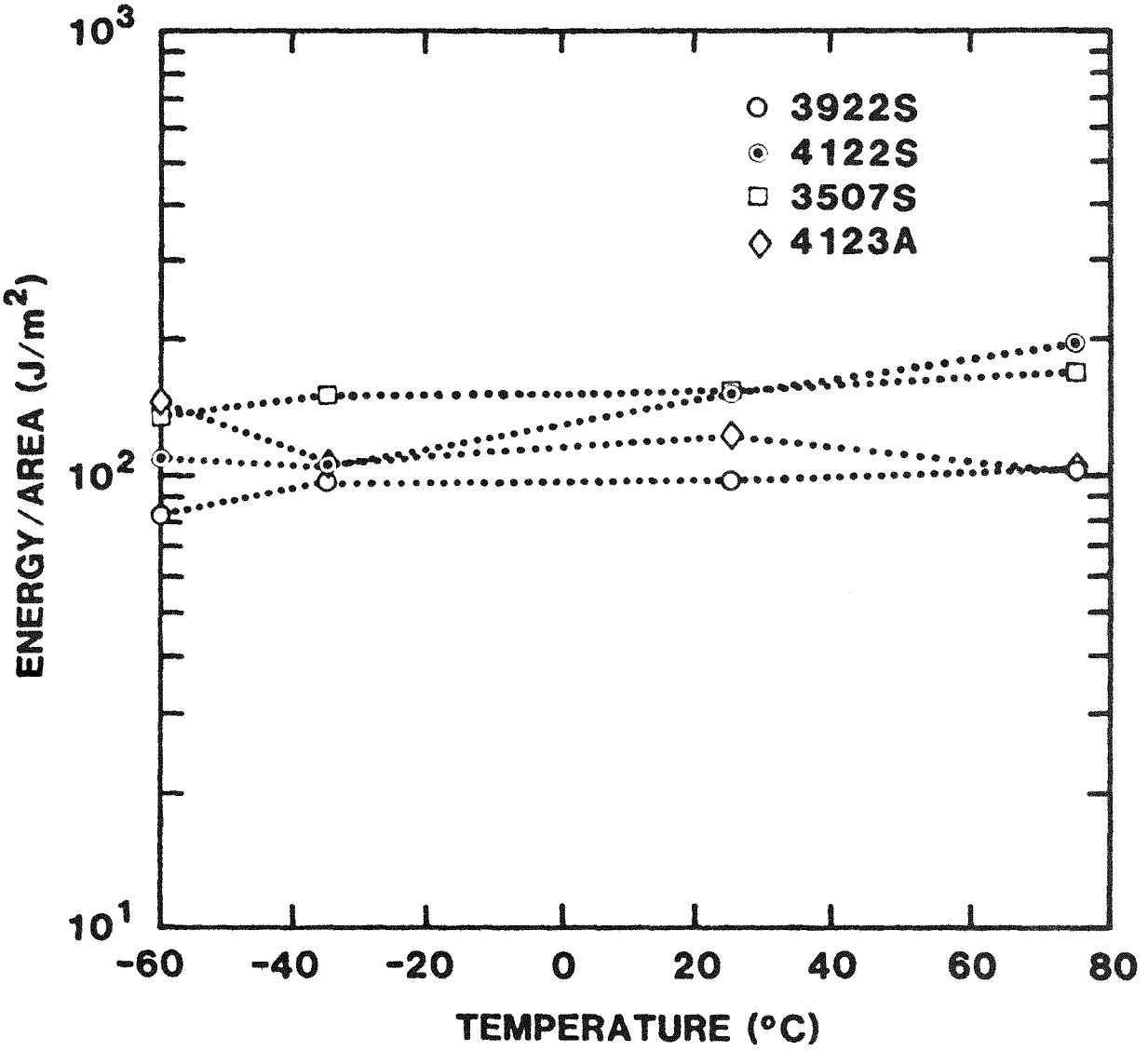

Figure 10

Energy of fragmentation versus temperature for each of the four virgin materials.

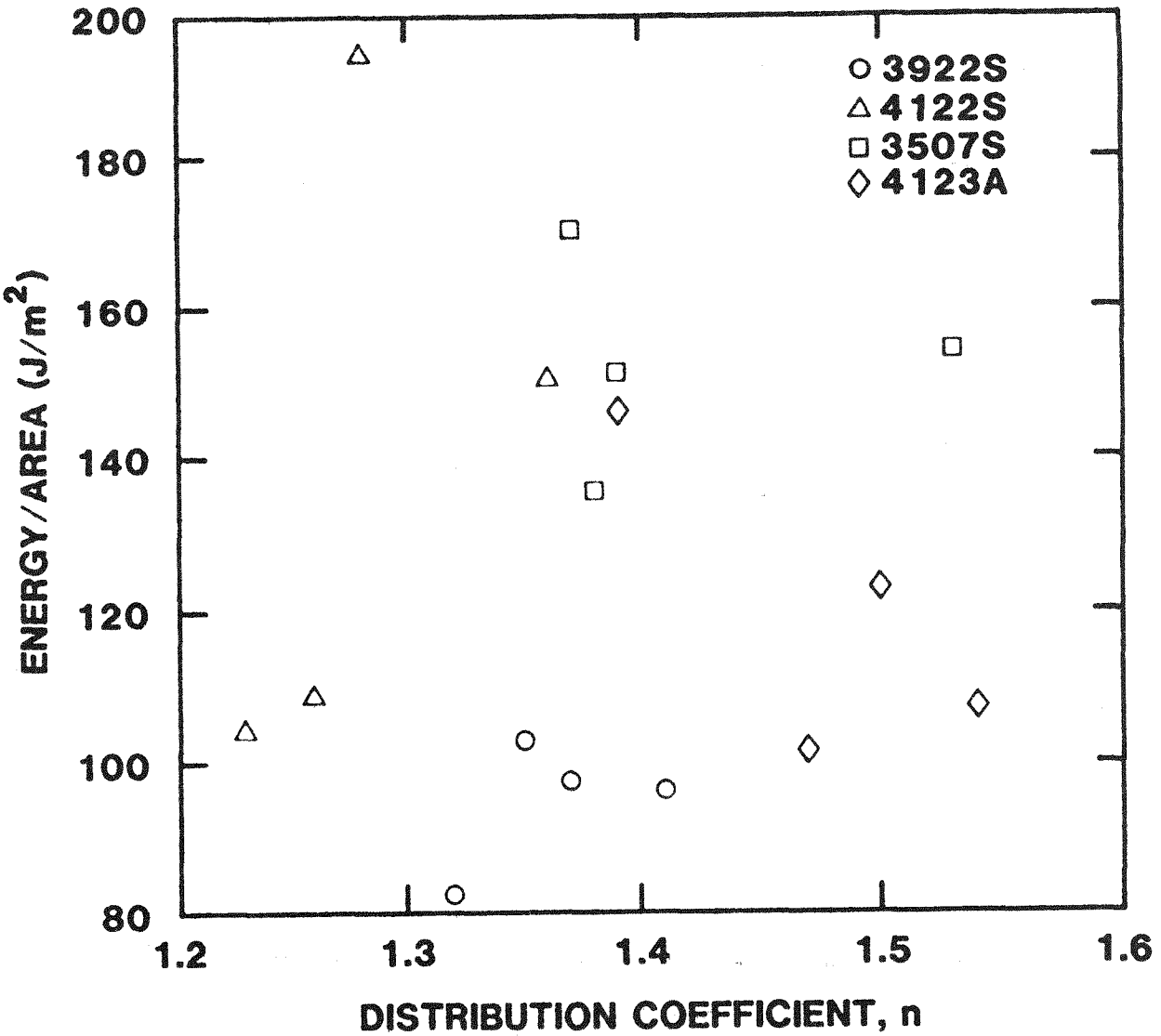

Figure 11

Energy of fragmentation versus distribution shape parameter, n, for virgin materials at four different temperatures.

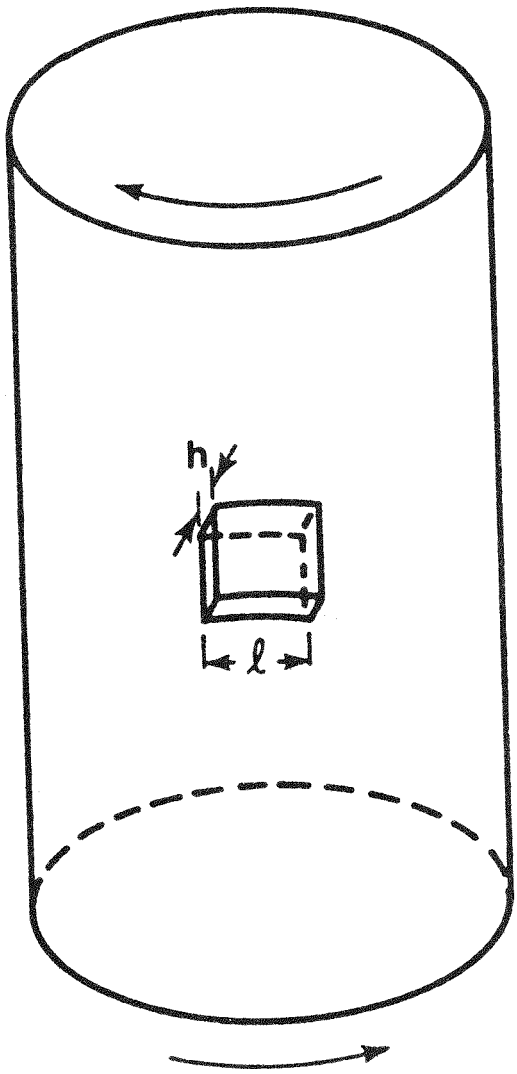

Figure 12

Schematic drawing of potential fragment being formed in specimen during dynamic test.

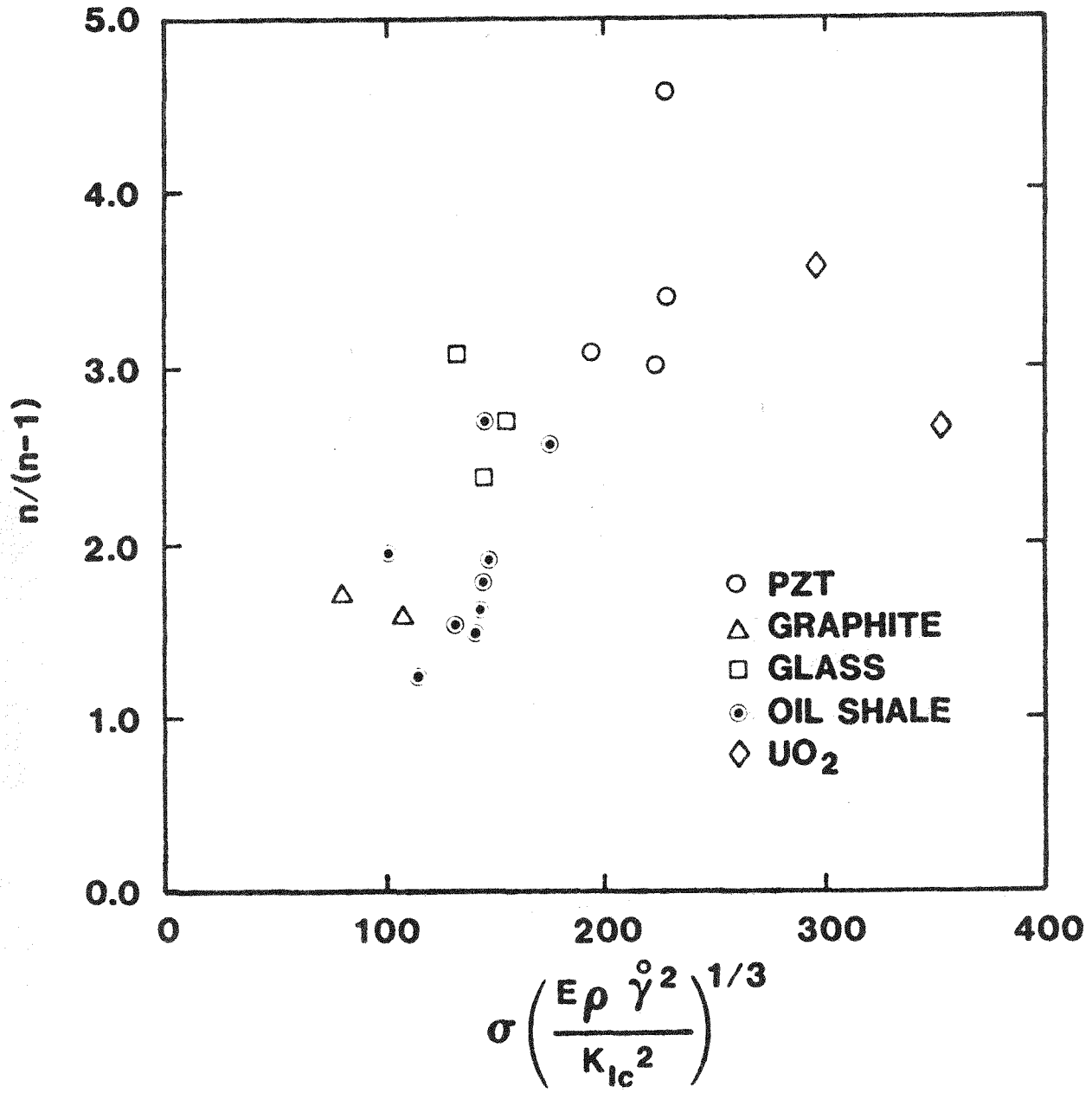

Figure 13

Fragment distribution shape parameter versus material parameter (relation (16)) for a variety of materials.

Distribution: (UC-13)

1000 J. K. Galt
1500 W. Herrmann
1510 W. Herrmann, Actg.
1520 D. J. McCloskey
1524 K. W. Schuler
1530 L. W. Davison
1534 J. R. Assay
1534 D. E. Grady (5)
1534 D. S. Drumheller
1534 L. Chhabildas
1534 T. Trucano
1540 W. C. Luth
1541 H. C. Hardee
1542 B. M. Butcher
1542 L. S. Costin (15)
1542 D. W. Hannum
1542 D. J. Holcomb
1542 A. K. Jones
1542 M. J. McNamee
1542 W. A. Olsson
1542 R. H. Price
1542 M. E. Shields
1542 S. J. Spence
1542 L. W. Teufel
1542 W. R. Wawersik
1542 D. H. Zeuch
1542 J. A. Zirzow
1543 T. M. Gerlach
1845 J. J. Mecholsky
2510 D. H. Anderson
2511 J. J. Marron
2513 J. E. Kennedy
2515 P. D. Wilcox
2520 H. J. Saxton
2521 C. P. Ballard
2521 R. H. Dungan
3141 L. J. Erickson (5)
3151 W. L. Garner (3)
3154-3 C. H. Dalin
for DOE/TIC